JOURNAL OF COMPUTATIONAL PHYSICS 23, 343–363 (1977)

An Implicit Finite-Difference Method for Solving the Navier–Stokes Equation Using Orthogonal Curvilinear Coordinates

TIN-KAN HUNG

Department of Civil Engineering and Department of Neurosurgery, University of Pittsburgh, Pittsburgh, Pennsylvania 15261

AND

THOMAS D. BROWN*

Department of Mechanical Engineering and Biotechnology Program, Carnegie–Mellon University, Pittsburgh, Pennsylvania 15213

Received December 29, 1975; revised September 1, 1976

Orthogonal curvilinear mesh networks are generated numerically between the wavy walls of two-dimensional peristaltic channels. A dual iterative procedure is developed to facilitate the conformal mapping, as well as to adjust mesh dimensions when necessary to fit the boundaries of the flow region. An implicit finite-difference technique is employed to obtain transient solutions of the Navier–Stokes equations. The effects of initial conditions on the flow establishment are discussed, along with considerations of numerical accuracy. The effects of certain nonconservative difference forms of the governing equations are explored. A calculated velocity field for a two-dimensional nonlinear peristaltic flow is supported by laboratory flow observation. The present method is applicable for laminar flow in a nonuniform channel with or without wall peristalsis.

1. INTRODUCTION

In recent years there has been considerable progress in developing computational techniques to solve the equations of fluid motion in regions with curved or irregularly shaped boundaries. Contributions have come from such diverse branches of physics and engineering as nuclear reactor design, meteorology, aerodynamics, and physiological flow simulation. Several ingenious and sophisticated methods have been presented to treat irregular boundaries such as free surfaces [7, 25], fluid–fliud interfaces [16], and the slip condition at a solid boundary [23, 24]. For the nonslip condition, however, curved boundaries have usually been approximated by irregular mesh. Ad hoc nonuniform mesh schemes are effective when judiciously applied [12] but the programming logic is complicated. Moreover, numerical instabilities may arise because of large local variations in mesh sizes, and accuracy is adversely affected when the true physical boundary conditions are adjusted to accomodate the computational mesh.

* Present address: Orthopaedic Research Laboratory, University of Pittsburgh, Pittsburgh, Pennsylvania 15261.

ISSN 0021-9991

Body-fitted orthogonal grids have been constructed by several investigators using conformal mapping to transform a curved region into a rectangular polygon. Barfield [3] employed the complex Green's function to map an irregular flow region into the unit circle, and then onto the edges of a rectangular polygon through a Schwarz–Christoffel transformation. He deemed it advisable to divide "elongated" physical regions into subregions in order to minimize numerical errors in the boundary mapping. Interior mesh points were then determined by point-successive over-relaxation of the inverse Laplace equations, and an interpolative technique was used to match the mesh lines at the subregion interfaces. A somewhat different body-fitted mesh was generated by Winslow [26]; his technique employed linear interpolation to distribute mesh nodes along boundaries and interfaces, and then mapped a non-uniform triangular mesh onto a regular array of triangles in the transformed plane. In an early work of Thom and Apelt [20], orthogonal mesh networks coincident with the equipotential lines and streamlines of potential flow were constructed. The Laplace equation was first solved iteratively to determine values of one coordinate variable (e.g., x) both in the interior of the transformed region and along its boundaries. The conjugate coordinate variable (y) was then determined by integration using the Cauchy–Riemann condition. With symmetromorphic figures (i.e., square mesh in the transformed plane), they noted that for some geometries it was not always possible to obtain a mesh network properly fitted to the physical region (e.g., part of a mesh may protrude through a segment of the boundary.) In the present study, we have extended Thom and Apelt's procedures to select a rectangular mesh which does fit all the boundaries. Also, a dual iterative procedure has been developed to reduce errors associated with the solution of y in Thom and Apelt's method.

Various techniques for generating body-fitted nonorthogonal meshes have been reported [2, 4, 21]. In such coordinate systems, extra terms must be added to the conservation equations, thus increasing the complexity of coding and the computer time required per iteration. In some situations, however, the greater flexibility of zoning afforded by nonorthogonal mesh may offset this handicap, especially if a particular mesh structure speeds convergence, or if increased resolution is desired in critical regions such as boundary layers.

Using potential flow nets fitted to curvilinear boundaries, Thom [19] in 1933 determined the stream function from the vorticity–transport equation for slow viscous steady flow around a circular cylinder. Also through laborious hand calculations, the numerical solutions for higher Reynolds numbers (up to 1000) were reported by Allen and Southwick [1]. Other geometries, such as flow through channel constrictions and between doubly-infinite rows of cylinders, were considered by Thom and Apelt [20]. A similar solution to the vorticity–transport equation was employed by Lee and Fung to analyze the flow of blood in locally constricted tubes at small Reynolds numbers [14].

Using the Arbitrary Lagrangian Eulerian (ALE) method, in which integral forms of the continuity and momentum equations were solved for each cell in a mesh of arbitrarily shaped quadrilaterals, Daly [27] studied pulsatile flow through smoothly curved stenoses. Peskin [28] employed a rectangular mesh to treat flow in regions

containing immersed irregular boundaries which interacted with the fluid, replacing the boundary by an equivalent field of forces defined at the nearby mesh nodes.

Recently, a steady solution in orthogonal coordinates using the primitive variables (velocity and pressure) to treat the problem of unidirectional coolant flow between nuclear fuel rod bundles was reported by Meyder [15]. Thompson *et al.* [22] employed a generalized nonorthogonal coordinate system to solve the vorticity–transport equation for flows around several bodies. Their boundary vorticity was determined by a modified false-position algorithm which included the Jacobian of the coordinate transformation. A detailed formulation which coupled the heat equation with velocity and pressure in a generalized coordinate system was given by Gal-Chen and Somerville [5, 6]. They employed a linear coordinate transformation to study transient thermally driven atmospheric convection up a two-dimensional mountainside, using a free slip/rigid condition to treat the lower boundary.

Unsteady flows through curved and flexible-walled tubes of irregular geometry are inherent in the study of biological flows [10]. An interesting case is peristaltic pumping, where the incompressible fluid contents of a distensible-walled tube are transported in bolus form (i.e., as "lumps" of fluid) by means of waves of transverse deformation propagated along the walls. This pumping mechanism characterizes the transport processes in the ureters and the gastrointestinal tract, and has implications for the design of improved roller pumps and heart-lung machines [13].

In this study, an implicit finite-difference method is used to obtain the velocity and pressure fields in orthogonal curvilinear coordinates for two-dimensional peristaltic flows. The steady-state solution is obtained expediently through the proper selection of initial conditions. The method is well suited for time-dependent flow in nonuniform channels with or without wall peristalsis.

2. Generation of Orthogonal and Analytical Curvilinear Mesh

A numerical procedure is developed here to generate an orthogonal curvilinear coordinate system (α, β) which maps the irregular channel region R into a rectangular region R' (Fig. 1). The geometry of the channel walls is prescribed by the function $g(x)$. Two types of wavy boundaries are considered:

(1) The periodic case: The channel walls are periodic in the physical plane (x, y), in which case the repeating region of interest in R can be prescribed a priori.

(2) The nonperiodic case: The region R is characterized by a single wall wave on an otherwise uniform channel.

For computational flow simulations, a simple orthogonal curvilinear mesh can be taken from an inverse solution of the Laplace equations

$$\nabla^2 x = \frac{\partial^2 x}{\partial \alpha^2} + \frac{\partial^2 x}{\partial \beta^2} = 0, \tag{1}$$

$$\nabla^2 y = \frac{\partial^2 y}{\partial \alpha^2} + \frac{\partial^2 y}{\partial \beta^2} = 0, \tag{2}$$

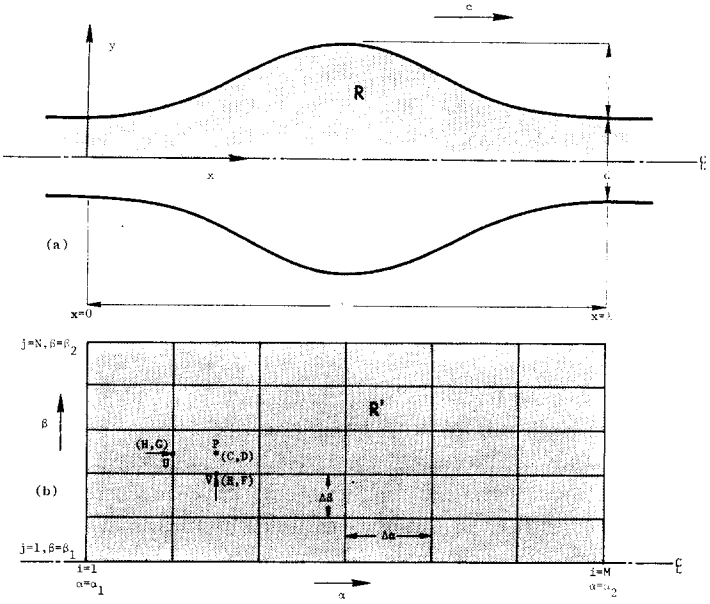

FIG. 1. (a) Definition sketch of the physical region R. (b) Mesh structure in the transformed space R'.

where α and β can be considered as the equipotential lines and streamlines, respectively, for an inviscid flow. The boundary conditions for solving α and β are

$$\beta\,|_{\text{wall}} = \beta_2 = \text{constant}; \qquad \partial\alpha/\partial n\,|_{\text{wall}} = 0, \tag{3}$$

where $\partial/\partial n$ indicates the normal derivative. The remaining boundary conditions (i.e., at the inlet and outlet sections of the channel) will be specified later.

If a pair of wavy walls is symmetric with respect to the axial plane of the channel, the region R can be reduced to that bounded by the conduit wall, the axis, and the sections $x_1 = 0$ and $x_2 = \lambda$. When R is mapped onto the region R' in the α–β plane (see Fig. 1), the choice of $(\beta_2 - \beta_1)$ corresponds to specifying the discharge of an inviscid flow through the channel. Such a choice uniquely determines the potential difference $(\alpha_2 - \alpha_1)$, where x_1 maps onto α_1, and x_2 maps onto α_2. The numerical value of $(\alpha_2 - \alpha_1)$ is not yet known, although it is coupled with $(\beta_2 - \beta_1)$, $(x_2 - x_1)$, and the solution of Eqs. (1) and (2). For a nonperiodic wavy channel region, $(\alpha_2 - \alpha_1)$ could be chosen such that the mesh size $\Delta\alpha$ is equal to the mesh size $\Delta\beta$, with an integral number of meshes M in the α-direction. In this case, neither α_1 nor α_2 has to be aligned with a predetermined x. These conditions permit straightforward solution of Eq. (2) in a square or rectangular mesh in the transformed plane, as described by Thom and Apelt [20] using an inverse method. For flow in a periodic wavy channel, the equipotential line α_1 is specified to be at $x = x_1$, and α_2 at $x = x_2$. An integral number of symmetromorphic meshes ($\Delta\alpha = \Delta\beta$), however, cannot generally be chosen, as there might be a partial overlap of the last square mesh at

one end (x_2, for example) of the boundary. That is, the difference ($\alpha_2 - \alpha_1$) is not known, but is a part of the solution.

Should an analytical function or mesh not necessarily be sought, the boundary condition α_2 and the numbers M and N of mesh in the α and β directions may be chosen a priori before solving Eqs. (1) and (2). The orthogonal meshes (α, β) thus obtained do not necessarily represent, respectively, the potential and stream functions. The potential function ϕ, however, will be solved from

$$\nabla^2\phi = \frac{1}{h_1 h_2}\left[\frac{\partial}{\partial\alpha}\left(\frac{h_2}{h_1}\frac{\partial\phi}{\partial\alpha}\right) + \frac{\partial}{\partial\beta}\left(\frac{h_1}{h_2}\frac{\partial\phi}{\partial\beta}\right)\right] = 0, \tag{4}$$

where h_1 and h_2 are the metrical coefficients, defined as

$$h_1 = \left[\left(\frac{\partial x^*}{\partial\alpha}\right)^2 + \left(\frac{\partial y^*}{\partial\alpha}\right)^2\right]^{1/2}; \qquad h_2 = \left[\left(\frac{\partial x^*}{\partial\beta}\right)^2 + \left(\frac{\partial y^*}{\partial\beta}\right)^2\right]^{1/2}. \tag{5}$$

The velocity components in the α and β directions derived from this potential are

$$u = \frac{1}{h_1}\frac{\partial\phi}{\partial\alpha} \qquad \text{and} \qquad v = \frac{1}{h_2}\frac{\partial\phi}{\partial\beta}. \tag{6}$$

The boundary conditions for Eq. (4) at the wall and the longitudinal axis, in the moving frame, are

$$\left.\frac{\partial\phi}{\partial\beta}\right|_{\beta=\beta_2} = 0 \qquad \text{and} \qquad \left.\frac{\partial\phi}{\partial\beta}\right|_{\beta=\beta_1} = 0, \tag{7, 8}$$

indicating, respectively, that the velocity $\vec{V}$ is tangent to the wall element $d\mathbf{S}$ at the wall, and that the flow is symmetric about the longitudinal axis.

When the Cauchy–Riemann condition is not required, it will be observed that an orthogonal curvilinear coordinate system will remain orthogonal under multiplication of either or both coordinate variables by respective constants. Because of this invariance, one can simply set $\Delta\alpha$ and $\Delta\beta$ equal to unity.

The numerical procedures for solving Eq. (4) can be bypassed if the orthogonal coordinate functions (α, β) are also analytical. In this study, a numerical method has been developed to solve Eqs. (1) and (2) along with the determination of the boundary condition α_2 or ($\alpha_2 - \alpha_1$). Also different from the method of Thom and Apelt, a dual iterative technique is employed to improve computational accuracy. The numerical procedure is described as follows.

1. For preselected values of $\Delta\beta$ and $\Delta\alpha$, Eq. (1) is solved iteratively by a finite-difference method with a prescribed boundary x. Notice that except on both ends (x_1 and x_2) the distribution of x on the wall was assumed at this stage. An iterative procedure is then applied to solve Eq. (1) for x on the wall between x_1 and x_2 using a backward finite-difference scheme in the β direction; values for x along the center line are determined iteratively from the average values of x at neighboring nodes using the well-known "twenty" formula [20].

2. Values of y on the wall are calculated from the geometry $g(x)$ of the wall. New inlet and outlet values of y are then determined from the fact that x and y are conjugate functions in R', i.e.,

$$y_2 - y_1 = \int_1^2 (\partial x/\partial \alpha)\, d\beta, \tag{9a}$$

and

$$x_2 - x_1 = -\int_1^2 (\partial y/\partial \alpha)\, d\beta. \tag{9b}$$

Equation (9a) is approximated to fourth order in $\Delta\alpha$ and $\Delta\beta$ by Lagrangian formulas of the type

$$\begin{aligned} y_{i,j} = y_{i,j-1} + \frac{1}{24}\Big\{&\Big[-22\frac{\Delta\beta}{\Delta\alpha} - \Big(\frac{\Delta\beta}{\Delta\alpha}\Big)^3\Big](x_{i,j} + x_{i,j-1}) \\ &+ \Big[36\frac{\Delta\beta}{\Delta\alpha} + 3\Big(\frac{\Delta\beta}{\Delta\alpha}\Big)^3\Big](x_{i+1,j} + x_{i+1,j-1}) \\ &+ \Big[-18\frac{\Delta\beta}{\Delta\alpha} - 3\Big(\frac{\Delta\beta}{\Delta\alpha}\Big)^3\Big](x_{i+2,j} + x_{i+2,j-1}) \\ &+ \Big[4\frac{\Delta\beta}{\Delta\alpha} + \Big(\frac{\Delta\beta}{\Delta\alpha}\Big)^3\Big](x_{i+3,j} + x_{i+3,j-1})\Big\}. \end{aligned} \tag{10}$$

Because of the accumulated numerical errors, the integrated values of y for the wall at the inlet ($x = 0$) and the outlet ($x = \lambda$) do not coincide with those evaluated from the wall geometry. The difference is then distributed proportionately over the inlet and outlet sections. With these adjusted values of y on the inlet and outlet, Eq. (2) is solved for the interior y field. Notice that in Thom and Apelt's computation, all the interior y are calculated according to Eq. (9a), resulting in an accumulation of error at the distal end of the numerical integration.

3. A new conjugate x field is then determined using Eq. (9b) for all nodes, including those on the boundary of R'. Unless the previously evaluated x and y fields were indeed solutions of Eqs. (1) and (2) on R', the newly obtained x field will not be compatible with that iterated from Step 1. In fact, the value of $x_{M,j}$ may fall short of λ (too few meshes), or the values of $x_{M-1,j}$ may exceed λ (too many meshes). In such cases it becomes necessary to add or delete mesh(es) in the α-direction (i.e., set $M = M \pm 1$).

4. With the newly defined M, Steps 1 through 3 are repeated until the distributions of y on either end section (Step 2) have converged. Such convergence will be achieved when the x field satisfies Eq. (1) on R', which in turn is possible only if the previous y field determined from Step 2 is its conjugate.

5. When the x and y fields from the dual iterative procedure have converged, the main loop is exited. At this point, $x_{M-1,j} < \lambda < x_{M,j}$ for all j. A mean value $\bar{\alpha}_\lambda$ is then calculated by averaging the values of α interpolated at $x = \lambda$ for each value of j. We now adjust the cell dimension by setting $\Delta\alpha = \bar{\alpha}_\lambda/(M-1)$ while keeping $\Delta\beta$ unchanged. This new rectangular mesh has the property of mapping x_2 onto α_2 $(=\bar{\alpha}_\lambda)$, and permits straightforward solution of Eq. (1) with a Dirichlet condition for x at the downstream boundary of the flow regime.

Figure 2 shows orthogonal curvilinear meshes generated for periodic and discrete wall waves. Note that as the minimum channel gap d becomes small compared to the wavelength (in Fig. 2a, $d/\lambda = 0.209$), the ratio M/N of the number of meshes in the α-direction to the number in the β-direction becomes large for square mesh. It may become desirable to use elongated mesh cells (Fig. 2c); this is accomplished by selecting an integer smaller than $(M-1)$ for the denominator when adjusting the mesh dimension $\Delta\alpha$.

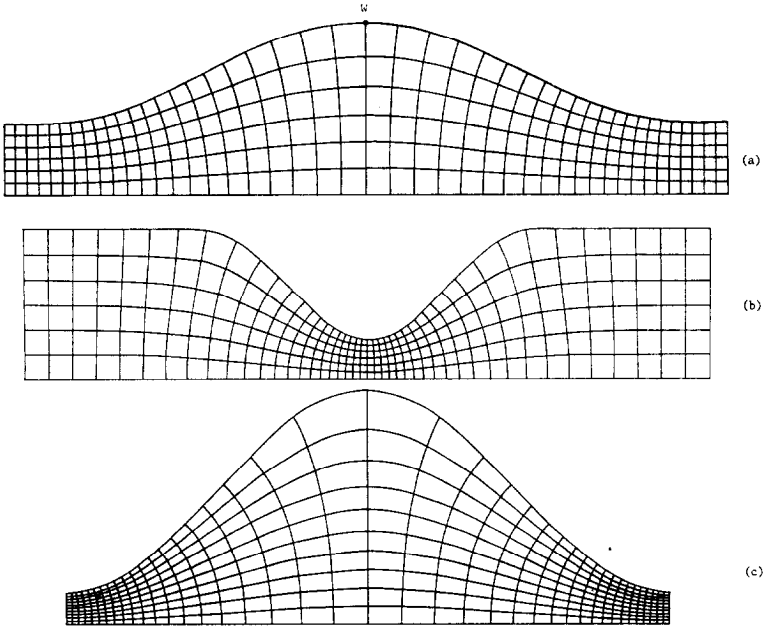

FIG. 2. Typical orthogonal curvilinear mesh networks.

Although it is recognized that the mesh size (in the physical plane) influences the resolution and accuracy of subsequent finite-difference calculations for the usual reasons, it should be pointed out that another consequence of grid coarseness here is the distortion of mesh orthogonality itself. Since x and y are analytic functions in the transformed space, an index of grid nonorthogonality can be obtained based upon the

Cauchy–Riemann condition ($\partial x/\partial\alpha = \partial y/\partial\beta$). For each mesh node, we check the Cauchy–Riemann condition by evaluating its residual:

$$RS = \frac{|(\partial x/\partial\alpha) - (\partial y/\partial\beta)|}{|\partial x/\partial\alpha| + |\partial y/\partial\beta|}. \tag{11}$$

The points of largest RS for sinusoidal-wall channels were found to be on the channel wall at the points of greatest y (refer to point W in Fig. 2a); this is precisely the point where the mesh is coarsest in the physical plane. For the mesh of Fig. 2a (seven vertical nodes) the value of RS at point W is found to be 1.75 %, while the value of RS averaged over all the mesh nodes is 0.61 %. If the number of vertica nodes is increased to 11, RS at point W decreases to 0.79 %, and the grid average of RS decreases to 0.25 %.

3. Peristaltic Potential Flow

In the case of a peristaltic wave, the geometry of the flow region remains unchanged if the coordinate system is moving with the celerity c of the wave:

$$x^* = x - ct; \qquad y^* = g(x^*). \tag{12}$$

At the onset of impulsive acceleration of a peristaltic wave, the predominant inertial effects result in an instantaneous irrotational flow which can be used as an initial condition for viscous computational flow simulation. The boundary conditions at the channel inlet and outlet are independent of the wall kinematics. In order to determine the peristaltic potential flow, either the longitudinal velocity or the distribution of ϕ has to be prescribed at both ends of the channel. When these boundary conditions are analogous to those for α the potential function ϕ becomes proportional to α. However, to accomodate numerical solutions for certain subregions, it is sometimes desirable to select boundary values of α which do not correspond to a meaningful irrotational flow.

To save computer time in obtaining steady solutions for peristaltic pumping against a given Kármán number, it has been found expedient to select an initial potential flow whose discharge is approximately that of the anticipated fully developed viscous flow. An appropriate potential drop for such an initial condition can be evaluated from

$$\phi_2 - \phi_1 = \frac{\alpha_2 - \alpha_1}{\beta_2 - \beta_1}\left[\bar{Q}_F - \frac{c}{(x_2^* - x_1^*)}\int_{x_1^*}^{x_2^*} g(z)\,dz\right]. \tag{13}$$

Here $\bar{Q}_F$ can be estimated from the sum of the flow rate due to free pumping and that of a Poiseuille flow between parallel walls under the prescribed Kármán number.

4. An Implicit Finite-Difference Method

For the two-dimensional flow of a Newtonian fluid, the Navier–Stokes equations in an orthogonal curvilinear coordinate system (α, β) take the form:

$$\begin{aligned}
&\frac{\partial U}{\partial T} + \frac{U}{h_1}\frac{\partial U}{\partial \alpha} + \frac{V}{h_2}\frac{\partial U}{\partial \beta} + \frac{UV}{h_1 h_2}\frac{\partial h_1}{\partial \beta} - \frac{V^2}{h_1 h_2}\frac{\partial h_2}{\partial \alpha} \\
&\quad = -\frac{1}{h_1}\frac{\partial P}{\partial \alpha} + \frac{1}{\mathbf{R}}\left\{\frac{1}{h_1 h_2}\left[\frac{\partial}{\partial \alpha}\left(\frac{h_2}{h_1}\frac{\partial U}{\partial \alpha}\right) + \frac{\partial}{\partial \beta}\left(\frac{h_1}{h_2}\frac{\partial U}{\partial \beta}\right)\right]\right. \\
&\qquad + \frac{2}{h_1}\frac{\partial V}{\partial \beta}\frac{\partial}{\partial \alpha}\left(\frac{1}{h_2}\right) - \frac{2}{h_2}\frac{\partial V}{\partial \alpha}\frac{\partial}{\partial \beta}\left(\frac{1}{h_1}\right) \\
&\qquad + U\left[\frac{1}{h_1}\frac{\partial}{\partial \alpha}\left(\frac{1}{h_1 h_2}\frac{\partial h_2}{\partial \alpha}\right) + \frac{1}{h_2}\frac{\partial}{\partial \beta}\left(\frac{1}{h_1 h_2}\frac{\partial h_1}{\partial \beta}\right)\right] \\
&\qquad \left. + V\left[\frac{1}{h_1}\frac{\partial}{\partial \alpha}\left(\frac{1}{h_1 h_2}\frac{\partial h_1}{\partial \beta}\right) - \frac{1}{h_2}\frac{\partial}{\partial \beta}\left(\frac{1}{h_1 h_2}\frac{\partial h_2}{\partial \alpha}\right)\right]\right\},
\end{aligned} \tag{14}$$

and

$$\begin{aligned}
&\frac{\partial V}{\partial T} + \frac{U}{h_1}\frac{\partial V}{\partial \alpha} + \frac{V}{h_2}\frac{\partial V}{\partial \beta} + \frac{UV}{h_1 h_2}\frac{\partial h_2}{\partial \alpha} - \frac{U^2}{h_1 h_2}\frac{\partial h_1}{\partial \beta} \\
&\quad = -\frac{1}{h_2}\frac{\partial P}{\partial \beta} + \frac{1}{\mathbf{R}}\left\{\frac{1}{h_1 h_2}\left[\frac{\partial}{\partial \alpha}\left(\frac{h_2}{h_1}\frac{\partial V}{\partial \alpha}\right) + \frac{\partial}{\partial \beta}\left(\frac{h_1}{h_2}\frac{\partial V}{\partial \beta}\right)\right]\right. \\
&\qquad + \frac{2}{h_2}\frac{\partial U}{\partial \alpha}\frac{\partial}{\partial \beta}\left(\frac{1}{h_1}\right) - \frac{2}{h_1}\frac{\partial U}{\partial \beta}\frac{\partial}{\partial \alpha}\left(\frac{1}{h_2}\right) \\
&\qquad + U\left[\frac{1}{h_2}\frac{\partial}{\partial \beta}\left(\frac{1}{h_1 h_2}\frac{\partial h_2}{\partial \alpha}\right) - \frac{1}{h_1}\frac{\partial}{\partial \alpha}\left(\frac{1}{h_1 h_2}\frac{\partial h_1}{\partial \beta}\right)\right] \\
&\qquad \left. + V\left[\frac{1}{h_2}\frac{\partial}{\partial \beta}\left(\frac{1}{h_1 h_2}\frac{\partial h_1}{\partial \beta}\right) + \frac{1}{h_1}\frac{\partial}{\partial \alpha}\left(\frac{1}{h_1 h_2}\frac{\partial h_2}{\partial \beta}\right)\right]\right\}.
\end{aligned} \tag{15}$$

In these equations, U and V denote dimensionless velocity components in the α- and β-directions, respectively, P denotes the dimensionless pressure, T denotes the time, and $\mathbf{R}$ denotes the Reynolds number, which is defined as $\rho cA/\mu$ (ρ = density, A = the amplitude of the channel wave and μ = viscosity). For peristaltic flow, the reference velocity was chosen to be the celerity c of the wall wave. The equation of continuity is

$$\frac{\partial}{\partial \alpha}(h_2 U) + \frac{\partial}{\partial \beta}(h_1 V) = 0. \tag{16}$$

The reference quantities by which the dimensionless variables (U, V, P, and T) are multiplied to obtain their dimensional equivalents are, respectively, c, ρc^2, and A/c.

A finite-difference formulation is employed to obtain an unsteady solution of Eqs. (14) to (16). In the α–β coordinate system, the curvilinear boundaries of the peristaltic channel region become straight-line segments (see Section 2), so that the flow region in the transformed plane may be subdivided into a rectangular mesh grid

(Fig. 1b). The grid has $(M-1) \times (N-1)$ cells, each of dimension $\Delta\alpha \times \Delta\beta$. The velocities U and V are defined, respectively, at the midsection of the left and bottom cell faces, with the pressure P defined at the cell center (refer to Fig. 1b). Notice that $U_{i,j}$ is located one-half mesh length to the left of $P_{i,j}$ while $V_{i,j}$ is one-half mesh length below $P_{i,j}$, analogous to the Cartesian mesh MAC cell structure. These notations require minimal code storage space (refer to the program of [9].)

Finite difference expressions for the velocity components at time $T = (n+1)\,\Delta T$ can be derived from momentum balances at time $T = (n + 1/2)\,\Delta T$:

$$U_{i,j}^{n+1} = \Delta T \left[\xi_{i,j} - \left(\frac{1}{h_1\,\Delta\alpha}\right)(P_{i,j}^{n+1/2} - P_{i-1,j}^{n+1/2})\right], \tag{17}$$

$$V_{i,j}^{n+1} = \Delta T \left[\eta_{i,j} - \left(\frac{1}{h_2\,\Delta\beta}\right)(P_{i,j}^{n+1/2} - P_{i,j-1}^{n+1/2})\right]. \tag{18}$$

Due to spatial variation of h_1 and h_2 in Eqs. (14) and (15), the expressions for $\xi_{i,j}$ and $\eta_{i,j}$, which include the convective and diffusive terms plus part of the local acceleration term, become considerably more lengthy than their Cartesian coordinate counterparts [9, 25].

The pressure at the cell center is obtained from a mass balance:

$$P_{i,j}^{n+1/2} = \left[\frac{\zeta_1}{(\Delta\alpha)^2} + \frac{\zeta_2}{(\Delta\beta)^2}\right]^{-1} \left[B_{i,j} + \frac{1}{(\Delta\alpha)^2}(\gamma_1 P_{i+1,j}^{n+1/2} + \gamma_2 P_{i-1,j}^{n+1/2}) + \frac{1}{(\Delta\beta)^2}(\gamma_3 P_{i,j+1}^{n+1/2} + \gamma_4 P_{i,j-1}^{n+1/2})\right]. \tag{19}$$

In Eq. (19), the ζ's and γ's are entirely geometric factors, invovling only combinations of the metrical coefficients; $B_{i,j}$ denotes a lengthy collection of ζ's and γ's (see Appendix A). The iterative solution procedure, adapted from that of Hung [9], is summarized in Fig. 3.

From examination of Eqs. (4) and (14) through (16), it can be seen that two simplifications in coding are possible. First, these equations are invariant to multiplication of either coordinate variable (α or β) by a constant (or equivalently, their difference forms are invariant to changes in either $\Delta\alpha$ or $\Delta\beta$), since the respective metrical coefficients will be changed inversely. Thus, when coding difference expressions such as those of Appendix B, the values of $\Delta\alpha$ and $\Delta\beta$ can be taken as unity, provided that the metrical coefficients are first scaled appropriately. A second simplification, available when an analytical (α–β) coordinate system is employed, arises from the fact that the Cauchy–Riemann condition requires that h_1 and h_2 at a given point be equal. Due to numerical error and to the relatively coarse grids used in the present study, the difference between the calculated values of h_1 and h_2, while negligable in regions of highly refined physical mesh, often approached 1 % in the regions of coarsest mesh. To avoid the possibility of introducing additional inaccuracy, it was decided to use the separate values of h_1 and h_2 in these equations. Ideally, an error analysis or test computation should be performed prior to implementing the second simplification.

Care must be taken to ensure rigorous momentum and mass conservation in Eqs. (17) to (19). It can be shown, for example, that in the limit as $\Delta\alpha$ and $\Delta\beta$ approach zero, the Poisson pressure iteration of Eq. (19) simplifies to

$$\nabla^2 P = \frac{1}{h_1 h_2}\left[\frac{\partial}{\partial\alpha}(h_2\xi) + \frac{\partial}{\partial\beta}(h_1\eta)\right]. \tag{20}$$

For finite mesh size, however, $\partial h_1/\partial\beta$ and $\partial h_2/\partial\alpha$ are nonvanishing; variations of as much as 10% in h_1 and h_2 were often noted within a single mesh segment for only moderately coarse (20×40) coordinate nets. It is therefore important (see Section 5), when substituting Eqs. (17) and (18) into Eq. (16), to use h values computed at the

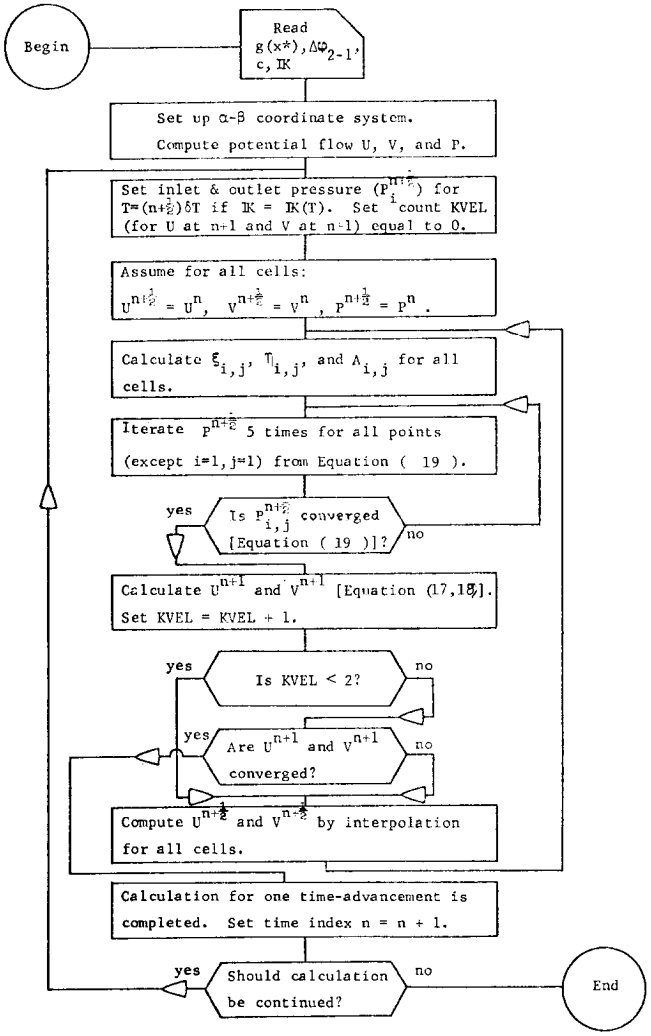

FIG. 3. Flow chart of implicit iterative procedure.

appropriate positions (e.g., h_1 at $U_{i,j}$) within the cell prior to substituting into the continuity equation. Figure 1b also shows the points of definition of the three necessary pairs of metrical coefficients (h_1, h_2), denoted, respectively, at the three points of evaluation by (H, G), (E, F), and (C, D).

The values for $U^{n+1/2}$, $V^{n+1/2}$, and $P^{n+1/2}$ needed for Eqs. (17) to (19) can be obtained by linear interpolation in time if ΔT is very small.

Since the peristaltic activity of the channel wall wave does not uniquely determine the resultant flow field, either the pressure or velocity distribution at the channel inlet and outlet must also be specified. If the pressure is prescribed at the inlet and at the outlet (with a pressure drop ΔP_{2-1}) and the lateral velocity component vanishes on both ends, the flow rate and other flow variables are the dependent variables. Because a characteristic fluid velocity upon which to base a Reynolds number is initially unavailable, it is convenient to characterize the flow in terms of the Kármán number

$$\mathbf{K} = \Delta p_{2-1} \rho A^2 / \mu^2. \tag{21}$$

Also, to extend the range of wave celerities to the general case, which includes $c = 0$ (i.e., flow through a stationary channel), it becomes appropriate to eliminate c as a reference variable in favor of μ. This is readily accomplished by setting

$$U = \frac{u\rho A}{\mu}, \qquad V = \frac{v\rho A}{\mu}, \qquad \text{and} \qquad P = \frac{p\rho A^2}{\mu^2}. \tag{22}$$

It can then be seen that the Reynolds number no longer appears explicitly in Eqs. (14) and (15). Instead, the wave celerity is now involved only in the boundary conditions for U and V along the wall.

The simplified treatment of the boundary conditions along curved walls is the main advantage afforded by the orthogonal curvilinear mesh. Since the cell faces can be made to coincide with segments of the curved boundary, the Cartesian velocity components (U' and V') at a point on the boundary at a cell midsection can be transformed to their α–β counterparts by

$$U = \frac{1}{h_1}\left(U' \frac{\partial x^*}{\partial \alpha} + V' \frac{\partial y^*}{\partial \alpha}\right). \tag{23}$$

The expressions for $\xi_{i,j}$ and $\eta_{i,j}$ for cells along the boundary are accordingly modified to allow for forward or backward spatial differencing (see Appendix B).

The evaluation of pressure for cells bordering on the boundaries of the transformed region R' requires one or more pressures outside of R'. The introduction of fictitious external cells [7] can be avoided by making direct use of the prescribed normal velocity component $V_{i,N}$ on the boundary [9]. For example, when iterating cells adjacent to the peristaltic wall ($j = N - 1$), Eq. (18) is used to obtain the "external" value

$$P_{i,N}^{n+1/2} = (\Delta\beta\, F_{i,N})[\eta_{i,N} - (V_{i,N}/\Delta T)] + P_{i,N-1}^{n+1/2}. \tag{24}$$

5. Development of Transient Flows

To illustrate the present implicit finite-difference method, transient flow processes within a peristaltic bolus from the initial condition of potential flow to asymptotically steady viscous flow were simulated. For the case of no net pressure drop from inlet to outlet (free pumping), the development of viscous flow was sought by solving Eqs. (14), (15), and (16) along with a nonslip boundary condition. The velocity components along an elastic wall, for which the wall elements are assumed to move only transversely, become in the moving coordinates:

$$U = -(cA/\nu)\sec[\tan^{-1}(dx^*/dy^*)]; \qquad V = 0, \tag{25}$$

respectively. If the wall is instead taken to be inextensible, local variations in the curvature of the wave require that wall elements move longitudinally as well as transversely. It can be shown [11] that in the moving reference frame this inextensibility condition results in a small perturbation in the U component, but that the V component is still zero.

The transient flow development can be appreciated from the instantaneous moving frame discharge between the bolus axis and the wall, or equivalently, the stream function ψ_w. A small discrepancy ϵ_ψ in the integrated flow rates passing through each constant $-\alpha$ section reflects the proper choice of mesh size and convergence criteria.

Due to the complexity of the finite-difference equations in the orthogonal curvilinear coordinate system, and also because of the varying mesh sizes in the physical plane, no rigorous analysis of stability or convergence criteria was undertaken. Instead, a series of trial runs was made, and the effects of the time increment ΔT, the pressure convergence criterion, and the velocity convergence criterion upon ψ_w, ϵ_ψ and the computation time were evaluated. Figure 4 shows the behavior of ψ_w and ϵ_ψ versus T

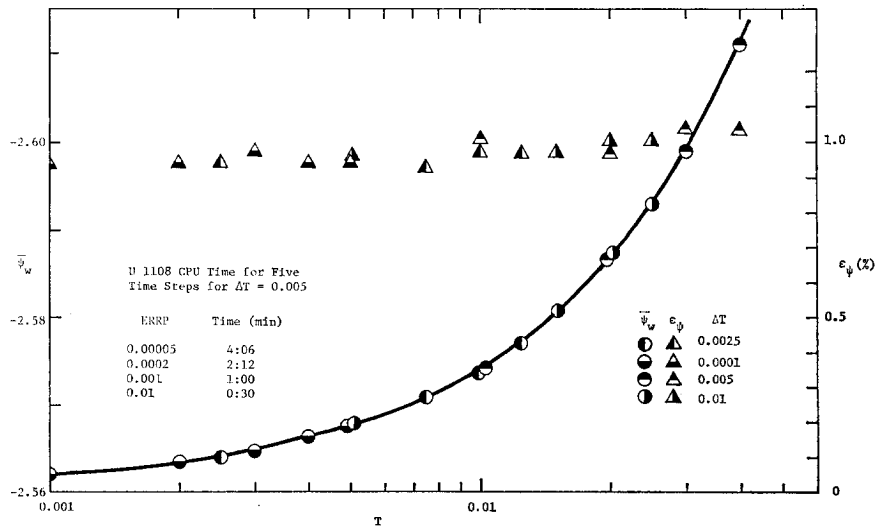

FIG. 4. Effect of time increment ΔT upon transient flow development. Single bolus, $A/\lambda = 0.164$, $d/\lambda = 0.209$, $\mathbf{R} = 2.35$, $\mathbf{K} = 0$. Initially, $\bar{\psi}_w = -2.561$ (potential flow).

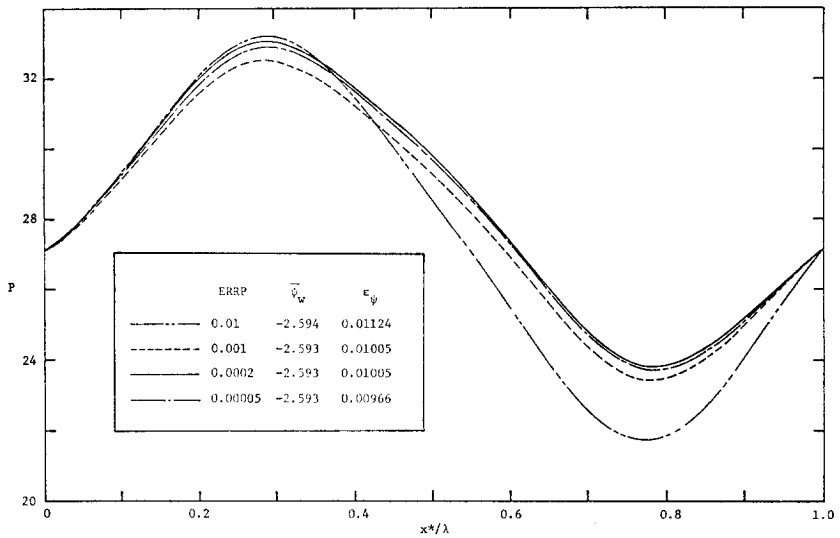

FIG. 5. Effects of pressure convergence criterion (ERRP) upon $\bar{\psi}_w$, ϵ_ψ, and the axial pressure distribution.

for various values of ΔT. It can be seen that neither ψ_w nor ϵ_ψ is sensitive to ΔT at this range. However, for $\Delta T = 0.01$, several small local irregularities were noted in the velocity field after five time increments. These numerical discrepancies disappeared when $\Delta T = 0.001$, 0.0025, or 0.005. It was therefore decided to use $\Delta T = 0.005$ for the remaining computations for this case (Fig. 4 through 8). The influence of small oscillations in the values of P was reduced by checking the relative accumulated difference in P every five pressure iterations. Figure 5 shows the effect of the pressure convergence criterion (ERRP) upon the axial distribution of pressure at $T = 0.025$. Selection of the convergence criterion for pressure iteration depends upon the anticipated characteristics of the transient flow processes. In the case of simulating an oscillatory flow, a more stringent criterion (e.g., checking the relative accumulated difference in P every 15 pressure iterations) is often desirable, so that the number of iterations of the velocity, and the total computational time required, will be reduced [9]. Should the convergence criterion for P be too coarse, numerical instability may occur. The number of iterations per time step for U and V have been found to

shown in Figs. 4, 5, and 6 demonstrate a typical set of calculations useful in the final selection of the convergence criteria and the magnitude of the time increment.

Although the mean values of ψ_w and ϵ_ψ (see table in Fig. 5) are insensitive to the pressure convergence criteria in this range, a significant error in the local pressures is noted for ERRP = 0.01. However, the small differences in the pressure field for ERRP = 0.00005, 0.0002, and 0.001 are purchased at the expense of significant increases in computing time. For this reason, a value of ERRP = 0.001 was chosen. For a constant Kármán number (in this case $\mathbf{K} = 0$), the number of pressure iterations

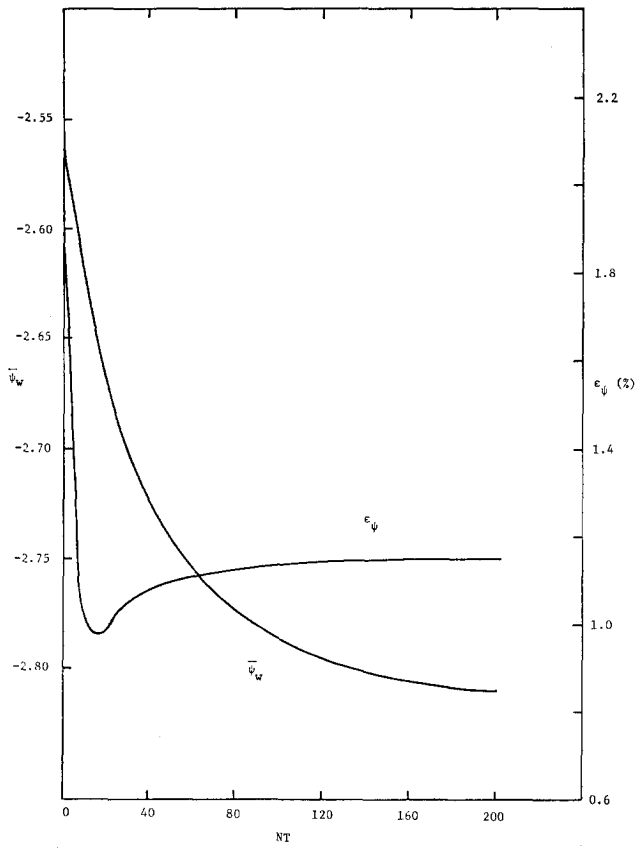

FIG. 6. Transition from potential flow to asymptotic steady state. Elastic wall condition, with $\Delta T = 0.005$.

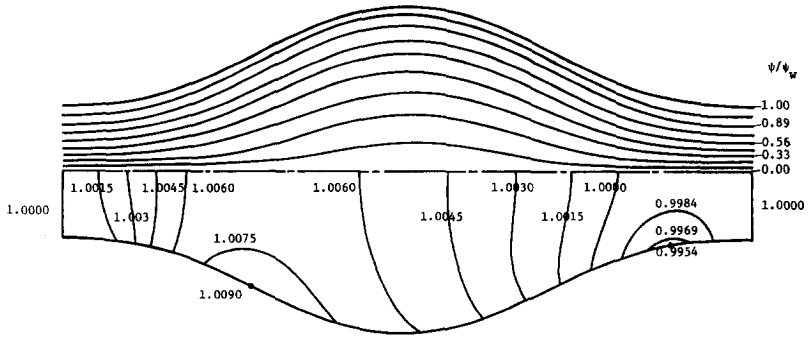

FIG. 7. Moving reference frame stream function (above) and pressure field (below) for asymptotically steady flow. Contours of pressure are normalized to $(P - P_{ref})/P_{ref}$, where $P_{ref} = 552$.

necessary to satisfy a given convergence criterion decreases as the time increases. In the case of oscillatory flow (i.e., **K** being a function of time) an increase in the required number of pressure iterations is anticipated.

The transition from potential flow to asymptotic steady flow is shown in Fig. 6. At $T = 1.00$ ($=200\,\Delta T$), the time rate of change of the discharge (or $|\,\Delta\psi_w/\Delta T\,|$) has decreased to 1.6% of its initial value; at this time the flow can be assumed to have reached steady state. The maximum value of ϵ_ψ is decreased from an initial value of 1.88% (potential flow) to 1.14% for steady flow at a characteristic Reynolds number of 2.35 (based on the mean velocity at section α_1). Contour plots of the asymptotically steady pressure field and the moving reference frame stream function are shown in Fig. 7. By comparison with the irrotational stream patterns (see coordinate mesh, Fig. 2a), the viscous solution exhibits much greater streamline curvature in the core. A region of high pressure is observed in the trailing half of the bolus near the point of maximum contractile wall velocity; a region of low pressure is centered somewhat forward of the point of most rapid wall distention. A comparison of the asymptotically steady ($NT = 300$) velocity vector field for an inextensible wall and the experimentally observed flow field [11] is shown in Fig. 8. The velocity vector $\vec{V}$ plot scaling factor

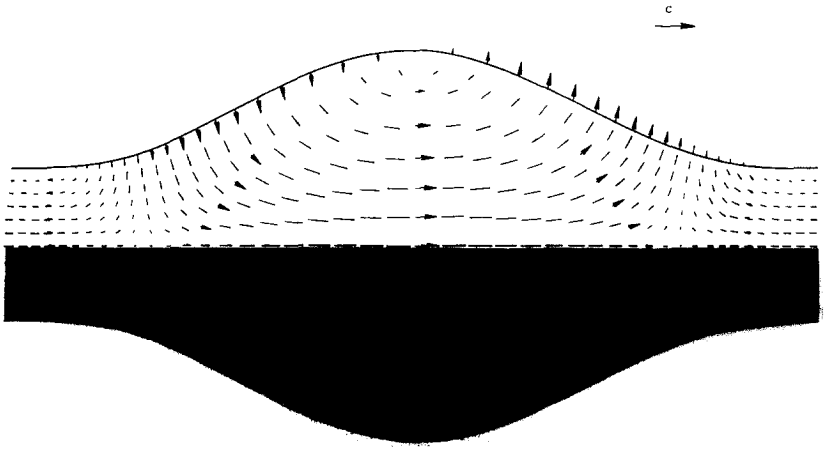

FIG. 8. Comparison of calculated velocity vector field (above) with experimentally observed flow pattern (below) for the inextensible wall boundary condition.

and the camera exposure time t_c were chosen such that a given tracer path length can be approximated by $|\,\vec{V}\,|\,t_c$. Detailed computational results for a variety of peristaltic flows, as well as experimental flow observations, are reported in the dissertation of Brown [29].

Further evidence of the validity of the present numerical method lies in the insensitivity of the steady solution to the initial conditions, as is to be expected physically (see Fig. 9). The asymptotically steady condition for this case is obtained from potential flows of different discharges. In the moving frame, ψ_w is negative, while

in the fixed frame the temporal mean discharge $\bar{Q}_F$ at a section is positive. The temporal variations in flow rate reflect the development of viscous effects from the initial irrotational flow patterns.

As is well known with MAC-type methods, a nonlinear instability arises in the momentum equations if the divergence of velocity ($\nabla \cdot V$) is taken to be identically

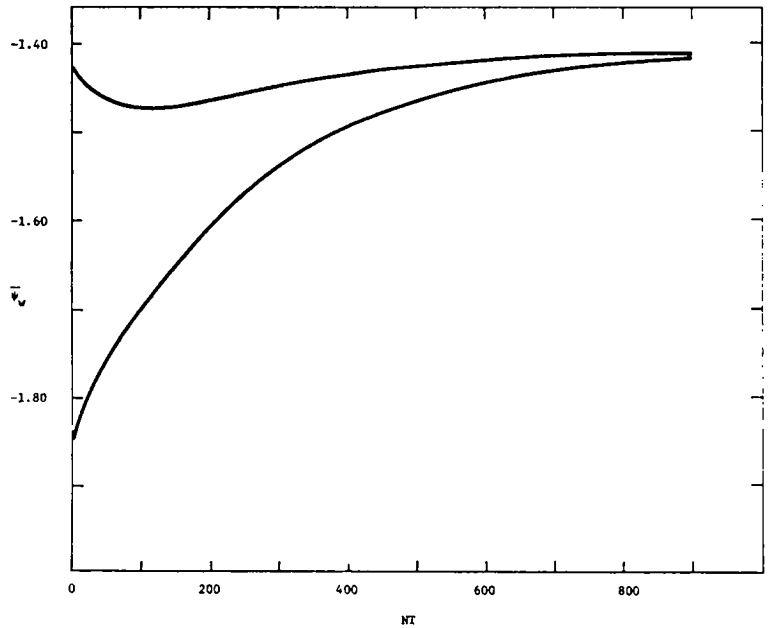

FIG. 9. Flow establishment under two initial conditions (potential flow discharge). $A/\lambda = 0.164$, $d/\lambda = 0.131$, $\mathbf{R} = 2.38$, $\mathbf{K} = 0$, $\Delta T = 0.0007$. Elastic wall condition.

zero at $T = (n)\,\Delta T$ as well as at $T = (n + 1)\,\Delta T$ [8, 17, 18]. However, similar computational experiments were not reported for the implicit scheme of [9]. Curves A and B in Fig. 10 depict the calculated flow rates for computations including and excluding, respectively, the term $(\nabla \cdot \vec{V})^n$ (i.e., at $T = (n)\,\Delta T$) in the pressure iteration. The corresponding wall stream function discrepancies are shown by curves a and b, reflecting smaller ϵ_ψ for the calculation which included $(\nabla \cdot \vec{V})^n$. Also shown in this figure are the effects of the improper (continuum limit) form of the finite difference equation for pressure (see Section 4). As indicated by curves C and c, a much more serious error is induced when the pressure is iterated from Eq. (20) instead of from Eq. (19). Although the velocity and pressure fields still settle, the resultant discharge (curve C) deviates markedly from curves A and B. The unacceptability of curve C is also clearly demonstrated by the large values of ϵ_ψ (curve c); the increase of two orders of magnitude (over curve a) implies that the gross continuity condition has been violated.

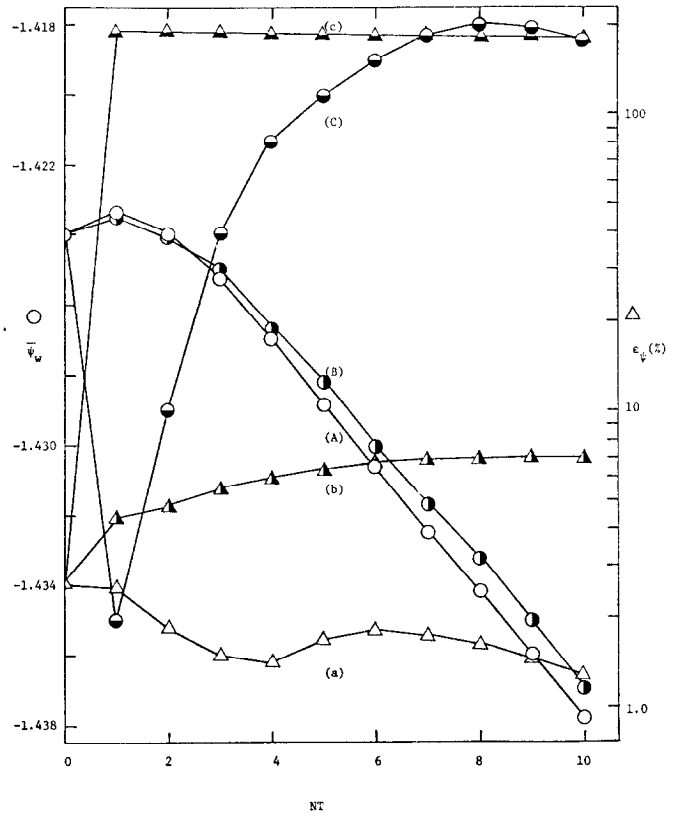

FIG. 10. The behavior of some nonconservative finite-difference formulations.

APPENDIX A: FINITE-DIFFERENCE EXPRESSIONS FOR THE ABBREVIATED TERMS IN EQ. (19)

For cells not bordering on the boundaries of the region R', the term $B_{i,j}$ takes the form

$$B_{i,j} = (1/\Delta\alpha)\{\xi_{i+1,j}[-D_{i,j} - \tfrac{1}{4}(D_{i+1,j} - D_{i-1,j})] + \xi_{i,j}[D_{i,j} - \tfrac{1}{4}(D_{i+1,j} - D_{i-1,j})]\} + (1/\Delta\beta) \times \{\eta_{i,j+1}[-C_{i,j} - \tfrac{1}{4}(C_{i,j+1} - C_{i,j-1})] + \eta_{i,j}[C_{i,j} - \tfrac{1}{4}(C_{i,j+1} - C_{i,j-1})]\}.$$

The six purely geometrical terms are

$$\zeta_1 = D_{i,j}\left(\frac{1}{H_{i+1,j}} + \frac{1}{H_{i,j}}\right) + \tfrac{1}{4}(D_{i+1,j} - D_{i-1,j})\left(\frac{1}{H_{i+1,j}} - \frac{1}{H_{i,j}}\right),$$

$$\zeta_2 = C_{i,j}\left(\frac{1}{F_{i,j+1}} + \frac{1}{F_{i,j}}\right) + \tfrac{1}{4}(C_{i,j+1} - C_{i,j-1})\left(\frac{1}{F_{i,j+1}} - \frac{1}{F_{i,j}}\right),$$

$$\gamma_1 = \left(\frac{1}{H_{i+1,j}}\right)[D_{i,j} + \tfrac{1}{4}(D_{i+1,j} - D_{i-1,j})],$$

$$\gamma_2 = \left(\frac{1}{H_{i,j}}\right)[D_{i,j} - \tfrac{1}{4}(D_{i+1,j} - D_{i-1,j})],$$

$$\gamma_3 = \left(\frac{1}{F_{i,j+1}}\right)[C_{i,j} + \tfrac{1}{4}(C_{i,j+1} - C_{i,j-1})],$$

$$\gamma_4 = \left(\frac{1}{F_{i,j}}\right)[C_{i,j} - \tfrac{1}{4}(C_{i,j+1} - C_{i,j-1})].$$

The differential expressions for ξ and η are, respectively,

$$\begin{aligned}\xi = {} & \frac{U^n}{\Delta T} - \frac{U}{H}\frac{\partial U}{\partial \alpha} - \frac{V}{G}\frac{\partial U}{\partial \beta} - \frac{UV}{HG}\frac{\partial H}{\partial \beta} + \frac{V^2}{HG}\frac{\partial G}{\partial \alpha} \\ & + \frac{1}{\mathbf{R}}\left\{\frac{1}{HG}\left[\frac{\partial}{\partial \alpha}\left(\frac{G}{H}\frac{\partial U}{\partial \alpha}\right) + \frac{\partial}{\partial \beta}\left(\frac{H}{G}\frac{\partial U}{\partial \beta}\right)\right]\right. \\ & + \frac{2}{H}\frac{\partial V}{\partial \beta}\frac{\partial}{\partial \alpha}\left(\frac{1}{G}\right) - \frac{2}{G}\frac{\partial V}{\partial \alpha}\frac{\partial}{\partial \beta}\left(\frac{1}{H}\right) \\ & + U\left[\frac{1}{H}\frac{\partial}{\partial \alpha}\left(\frac{1}{HG}\frac{\partial G}{\partial \alpha}\right) + \frac{1}{G}\frac{\partial}{\partial \beta}\left(\frac{1}{HG}\frac{\partial H}{\partial \beta}\right)\right] \\ & \left. + V\left[\frac{1}{H}\frac{\partial}{\partial \alpha}\left(\frac{1}{HG}\frac{\partial H}{\partial \beta}\right) - \frac{1}{G}\frac{\partial}{\partial \beta}\left(\frac{1}{HG}\frac{\partial G}{\partial \alpha}\right)\right]\right\}\end{aligned}$$

and

$$\begin{aligned}\eta = {} & \frac{V^n}{\Delta T} - \frac{U}{E}\frac{\partial V}{\partial \alpha} - \frac{V}{F}\frac{\partial V}{\partial \beta} - \frac{UV}{EF}\frac{\partial F}{\partial \alpha} + \frac{U^2}{EF}\frac{\partial E}{\partial \beta} \\ & + \frac{1}{\mathbf{R}}\left\{\frac{1}{EF}\left[\frac{\partial}{\partial \alpha}\left(\frac{F}{E}\frac{\partial V}{\partial \alpha}\right) + \frac{\partial}{\partial \beta}\left(\frac{E}{F}\frac{\partial V}{\partial \beta}\right)\right]\right. \\ & + \frac{2}{F}\frac{\partial U}{\partial \alpha}\frac{\partial}{\partial \beta}\left(\frac{1}{E}\right) - \frac{2}{E}\frac{\partial U}{\partial \beta}\frac{\partial}{\partial \alpha}\left(\frac{1}{F}\right) \\ & + U\left[\frac{1}{F}\frac{\partial}{\partial \beta}\left(\frac{1}{EF}\frac{\partial F}{\partial \alpha}\right) - \frac{1}{E}\frac{\partial}{\partial \alpha}\left(\frac{1}{EF}\frac{\partial E}{\partial \beta}\right)\right] \\ & \left. + V\left[\frac{1}{F}\frac{\partial}{\partial \beta}\left(\frac{1}{EF}\frac{\partial E}{\partial \beta}\right) + \frac{1}{E}\frac{\partial}{\partial \alpha}\left(\frac{1}{EF}\frac{\partial F}{\partial \alpha}\right)\right]\right\}.\end{aligned}$$

APPENDIX B: FINITE-DIFFERENCE BOUNDARY CONDITION FOR ξ

For cells bordering on the peristaltic wall ($j = N - 1$), the finite-difference boundary condition for ξ becomes

$$\begin{aligned}\xi_{i,j} = {} & (U^n_{i,j}/\Delta T) - [(U_{i,j}/H_{i,j})(1/2\Delta\alpha)(U_{i+1,j} - U_{i-1,j})] \\ & - [(1/8G_{i,j})(V_{i,j+1} + V_{i,j} + V_{i-1,j} + V_{i-1,j+1})(2/3\Delta\beta)\end{aligned}$$

$$\times (4U_{i,j+1} - 3U_{i,j} - U_{i,j-1})] - [(U_{i,j}/8\Delta\beta\, H_{i,j}G_{i,j})$$
$$\times (V_{i,j+1} + V_{i,j} + V_{i-1,j} + V_{i-1,j+1})(3H_{i,j} - 4H_{i,j-1} + H_{i,j-2})]$$
$$+ [(1/32\Delta\alpha\, H_{i,j}G_{i,j})(V_{i,j+1} + V_{i,j} + V_{i-1,j} + V_{i-1,j+1})^2\,(G_{i+1,j} - G_{i-1,j})]$$
$$+ 1/\mathbf{R}\{\{(1/H_{i,j}^2\,\Delta\alpha^2)[(U_{i+1,j} - 2U_{i,j} + U_{i-1,j})$$
$$+ (1/4G_{i,j})(U_{i+1,j} - U_{i-1,j})(G_{i+1,j} - G_{i-1,j})$$
$$- (1/4H_{i,j})(U_{i+1,j} - U_{i-1,j})(H_{i+1,j} - H_{i-1,j})]$$
$$+ (1/G_{i,j}^2\,\Delta\beta^2)[(1/6)(3U_{i,j-2} - 9U_{i,j} + 8U_{i,j+1} - 2U_{i,j-1})$$
$$- (1/6G_{i,j})(4U_{i,j+1} - 3U_{i,j} - U_{i,j-1})(3G_{i,j} - 4G_{i,j-1} + G_{i,j-2})$$
$$+ (1/6H_{i,j})(4U_{i,j+1} - 3U_{i,j} - U_{i,j-1})(3H_{i,j} - 4H_{i,j-1} + H_{i,j-2})]\}$$
$$- [(1/2\Delta\alpha\,\Delta\beta)(1/H_{i,j}G_{i,j}^2)(G_{i+1,j} - G_{i\ 1,j})$$
$$\times (V_{i,j+1} + V_{i-1,j+1} - V_{i,j} - V_{i-1,j})] + [(1/4\Delta\alpha\,\Delta\beta)(1/H_{i,j}^2G_{i,j})$$
$$\times (V_{i,j+1} + V_{i,j} - V_{i-1,j+1} - V_{i-1,j})(3H_{i,j} - 4H_{i,j-1} + H_{i,j-2})]$$
$$+ (U_{i,j}/H_{i,j}G_{i,j})\{(1/H_{i,j}\,\Delta\alpha^2)[(G_{i+1,j} - 2G_i + G_{i-1,j})$$
$$- (1/4G_{i,j})(G_{i+1,j} - G_{i-1,j})(G_{i+1,j} - G_{i-1,j})$$
$$- (1/4H_{i,j})(G_{i+1,j} - G_{i-1,j})(H_{i+1,j} - H_{i-1,j})]$$
$$+ (1/G_{i,j}\,\Delta\beta^2)[(1/9)(2H_{i,j-3} + 3H_{i,j-2} - 12H_{i,j-1} + 7H_{i,j})$$
$$- (1/4G_{i,j})(3H_{i,j} - 4H_{i,j-1} + H_{i,j-2})(3G_{i,j} - 4G_{i,j-1} + G_{i,j-2})$$
$$- (1/4H_{i,j})(3H_{i,j} - 4H_{i,j-1} + H_{i,j-2})(3H_{i,j} - 4H_{i,j-1} + H_{i,j-2})]\}$$
$$+ (V_{i,j+1} + V_{i,j} + V_{i-1,j} + V_{i-1,j+1})(1/16H_{i,j}G_{i,j}\,\Delta\alpha\,\Delta\beta)\{(1/H_{i,j})$$
$$\times [(3H_{i+1,j} - 4H_{i+1,j-1} + H_{i+1,j-2} - 3H_{i-1,j} + 4H_{i-1,j-1} - H_{i-1,j-2})$$
$$- (1/G_{i,j})(3H_{i,j} - 4H_{i,j-1} + H_{i,j-2})(G_{i+1,j} - G_{i-1,j})$$
$$- (1/H_{i,j})(3H_{i,j} - 4H_{i,j-1} + H_{i,j-2})(H_{i+1,j} - H_{i-1,j})]$$
$$+ (1/G_{i,j})[-(3G_{i+1,j} - 4G_{i+1,j-1} + G_{i+1,j-2} - 3G_{i-1,j}$$
$$+ 4G_{i-1,j-1} - G_{i-1,j-2}) + (1/G_{i,j})(G_{i+1,j} - G_{i-1,j})(3G_{i,j} - 4G_{i,j-1} + G_{i,j-2})$$
$$+ (1/H_{i,j})(G_{i+1,j} - G_{i-1,j})(3H_{i,j} - 4H_{i,j-1} + H_{i,j-2})]\}\}.$$

ACKNOWLEDGMENTS

The authors would like to express their appreciation to Dr. Hsing-Hwa Shih for his contributions during the early phase of problem formulation, and to Ms. Leslie Thompson for her secretarial assistance. NSF Grant GK-31514 to T.K.H., support for T.D.B. under NIH Training Grant GMO 1455, and the excellent services provided by the Computation Center of Carnegie–Mellon University are also acknowledged.

REFERENCES

1. D. N. G. ALLEN AND R. V. SOUTHWELL, *Quart. J. Mech. Appl. Math.* **8** (1955), 129–145.
2. A. A. AMSDEN AND C. W. HIRT, *J. Computational Phys.* **11** (1973), 348–359.
3. W. D. BARFIELD, *J. Computational Phys.* **5** (1970), 23–33.

4. W. D. BARFIELD, *J. Computational Phys.* **6** (1970), 417–429.
5. T. GAL-CHEN AND R. C. J. SOMERVILLE, *J. Computational Phys.* **17** (1975), 209–228.
6. T. GAL-CHEN AND R. C. J. SOMERVILLE, *J. Computational Phys.* **17** (1975), 276–310.
7. F. H. HARLOW AND J. E. WELCH, *Phys. Fluids* **8** (1965).
8. C. W. HIRT AND F. W. HARLOW, *J. Computational Phys.* **2** (1967), 114–199.
9. T. K. HUNG, Vortices in Pulsatile Flows, *in* "Proceedings of the Fifth International Congress on Rheology," Vol. 2, pp. 115–127, 1970.
10. T. K. HUNG, Development of Computational Methods for Biofluid Dynamics, *in* "ASCE National Structural Engineering Convention," Meeting preprint 2477, April, 1975.
11. T. K. HUNG AND T. D. BROWN, *J. Fluid Mech.* **73**, part 1 (1976), 77–96.
12. T. K. HUNG AND G. B. SCHUESSLER, "Computational Analysis as an Aid to the Design of Heart Valves," Chemical Engineering Progress Symposium Series Vol. 67, No. 114, 1971.
13. M. Y. JAFFRIN AND A. H. SHAPIRO, *Ann. Rev. Fluid Mech.* (1971).
14. J. S. LEE AND Y. C. FUNG, *J. Appl. Mech.* **37** (1970), 9–17.
15. R. MEYDER, *J. Computational Phys.* **17** (1975), 53–67.
16. H. I. PADMANEBHAM, W. J. AMES, J. F. KENNEDY, AND T. K. HUNG, *J. Engrg. Math.* **4** (1970).
17. S. A. PIACSEK AND G. P. WILLIAMS, *J. Computational Phys.* **6** (1970), 392–405.
18. P. J. ROACHE, "Computational Fluid Dynamics," Hermosa, Albuquerque, N.M., 1972.
19. A. THOM, *Proc. Royal Soc. Ser. A* **141** (1933).
20. A. THOM AND C. J. APELT, "Field Computations in Engineering and Physics," Van Nostrand, London, 1961.
21. J. F. THOMPSON, F. C. THAMES, AND C. W. MASTIN, *J. Computational Phys.* **15** (1974), 299–319.
22. J. F. THOMPSON, F. C. THAMES, R. L. WALKER, AND S. P. SHANKS, Numerical Solutions of the Unsteady Navier–Stokes Equations for Arbitrary Bodies Using Boundary-Fitted Curvilinear Coordinates, *in* "Arizona/AFOSR Symposium on Unsteady Aerodynamics, Tuscon, Ariz., March 18–20, 1975."
23. J. A. VIECELLI, *J. Computational Phys.* **4** (1969), 543–551.
24. J. A. VIECELLI, *J. Computational Phys.* **8** (1971), 119–143.
25. J. E. WELCH, F. H. HARLOW, J. P. SHANNON, AND B. J. DALY, "The MAC Method: A Computing Technique for Solving Viscous, Incompressible, Transient Fluid-Flow Problems Involving Free Surfaces," Report LA-3425, Los Alamos Scientific Laboratory, March, 1966.
26. A. M. WINSLOW, *J. Computational Phys.* **2** (1967), 149–172.
27. B. J. DALY, *J. Biomech.* **9**, 7 (1976), 465–475.
28. C. S. PESKIN, *J. Computational Phys.* **10** (1972), 252–271.
29. T. D. BROWN, "Computational and Experimental Studies of Two-Dimensional Nonlinear Peristaltic Pumping," Ph.D. Thesis, Carnegie–Mellon Univ., 1976.